Radiation Physics and Chemistry 155 (2019) 252–259

Contents lists available at ScienceDirect

Radiation Physics and Chemistry

journal homepage: www.elsevier.com/locate/radphyschem

Dose estimate for cone beam CT equipment protocols using Monte Carlo simulation in computational adult anthropomorphic phantoms

Maria R. Soares[a,b,h], William S. Santos[c,d,h], Lucio P. Neves[c,d,h], Ana P. Perini[a,c,d,h], Wilson O.G. Batista[e], Walmir Belinato[f,h], Ana F. Maia[g], Linda V.E. Caldas[a,*]

[a] Instituto de Pesquisas Energéticas e Nucleares, Comissão Nacional de Energia Nuclear (IPEN-CNEN/SP), SãoPaulo, SP, Brazil
[b] Fundação Universidade Federal de Rondônia (UNIR), Porto Velho, RO, Brazil
[c] Instituto de Física, Universidade Federal de Uberlândia, Uberlândia, MG, Brazil
[d] Programa de Pós-Graduação em Engenharia Biomédica, Faculdade de Engenharia Elétrica, Universidade Federal de Uberlândia, MG, Brazil
[e] Departamento de Tecnologia em Saúde e Biologia, Instituto Federal de Educação, Ciência e Tecnologia da Bahia, Salvador, BA, Brazil
[f] Departamento de Ensino, Instituto Federal de Educação, Ciência e Tecnologia da Bahia, Vitória da Conquista, BA, Brazil
[g] Departamento de Física, Universidade Federal de Sergipe (UFS), São Cristóvão, Sergipe, Brazil
[h] Ionizing Radiation Dosimetry in Medicine Group, Brazil

ARTICLE INFO

Keywords:
Monte Carlo simulation
CBCT
Dosimetry
Virtual anthropomorphic phantoms

ABSTRACT

Cone beam computed tomography (CBCT) has become essential for dental diagnoses in the last decade. This is supported by its low cost and low doses, when compared to medical CT. Following this increase in CBCT procedures, it is necessary to ensure the image quality within low radiation doses to the patients. This is an especially difficult challenge in CBCT, given the number of equipment models (more than 50), radiographic techniques that may be employed, and technical information not available to the users by the manufacturers. The objective of this study was to estimate the cancer risk, effective and absorbed doses in tissues and organs for CBCT protocols intended for dental use. Monte Carlo (MC) simulations were used to estimate these quantities in tissues and organs with radiological importance, as those suggested by the International Commission of Radiological Protection (ICPR) report ICRP 103. Five different fields of view (FOV) were simulated to i-Cat Classic CBCT, using the MCNPX code. The virtual anthropomorphic phantoms FASH3 (Female Adult MeSH) and MASH3 (Male Adult MeSH) were also used. The effective dose estimative was in the range 75.15–142.20 μSv. The largest contribution to the effective dose was from the salivary glands (17%), thyroid (27%) and remainder tissues (28%). The results of this work showed that the effective and absorbed doses in tissues/organs vary according to the FOV, exposure parameters, and the positioning of the beam, relative to the radiosensitive organs. Furthermore, for the same exposure conditions, women can exceed the total risk of cancer by 26–34%, when compared to men.

1. Introduction

In the late 1990s the cone beam computed tomography (CBCT) was inserted to diagnostic dental imaging (Mozzo et al., 1998; Koivisto et al., 2014). Since then, the use of CBCT has become essential for diagnosis of implants, use of dental appliances and dental surgeries (Morant et al., 2013). The CBCT produces a three-dimensional image of the facial skeleton and teeth of the patient (Abramovitch and Rice, 2014; Scarfe et al., 2012). During the examination, the field of view (FOV) has a relative proximity to radiosensitive organs. In addition, with the popularization of CBCT in dental radiology, several brands of equipment were manufactured (Abramovitch and Rice, 2014; Soares et al., 2015a). This opened a new area of research, with many dosimetric studies discussing the different parameters related to patient exposure, as tube voltage, current, exposure time, FOV, exposure angle, beam geometry and filtration (Morant et al., 2013; Soares et al., 2015a; Roberts et al., 2008; Qu et al., 2010; Rottke et al., 2013; Stratis et al., 2016).

To establish the risk of exposure in individuals, the effective dose should be estimated by calculating the absorbed dose in the tissues, and organs, at risk. This dosimetry is generally performed using thermoluminescent (TL) dosimeters or optically stimulated luminescent

* Corresponding author.
E-mail addresses: mrs@unir.br (M.R. Soares), william@ufu.br (W.S. Santos), lucio.neves@ufu.br (L.P. Neves), anapaula.perini@ufu.br (A.P. Perini), wilson.otto@ifba.edu.br (W.O.G. Batista), walmir@ifba.edu.br (W. Belinato), afmaia@ufs.br (A.F. Maia), lcadas@ipen.br (L.V.E. Caldas).

https://doi.org/10.1016/j.radphyschem.2018.06.038
Received 31 July 2017; Received in revised form 30 May 2018; Accepted 21 June 2018
Available online 27 June 2018
0969-806X/

(OSL) dosimeters in physical anthropomorphic phantoms. However, the dose distribution within the simulator may vary and is usually punctual, making it difficult to compare the various studies. Thus, to estimate the effective dose, and the dose deposited in tissues and organs, a large number of TLDs should be distributed in a physical anthropomorphic phantom (Stratis et al., 2016).

In such situations, when the measurements are impossible, or very difficult to carry out, numerical dosimetry is an optimal alternative approach. Monte Carlo (MC) techniques are employed to accurately simulate the doses from radiation transport through matter. It may be employed for different combinations of technical parameters of exposure, FOV, electric current, tube voltage, angle of rotation and positioning of the beam in relation to the patient organs (Morant et al., 2013; Stratis et al., 2016). Among its several advantages, one is related to the lower uncertainties, which may be lower than those from experimental TL measurements.

In recent years, several international organizations have developed models to estimate cancer risk for ionizing radiation exposure, with low linear energy transfer (LET), using data from survivors of the atomic bombs of the Japanese cities of Hiroshima and Nagasaki. Among these organizations, the International Commission on Radiological Protection (ICRP) (ICRP Publication 103, 2007) and the National Research Council (BEIR VII) (National Research Council, 2006) may be included. In their study, the organizing committee performed a thorough analysis of the health effects of people exposed to low levels of ionizing radiation (National Research Council, 2006).

The aim of this study was to obtain the cancer risk, as well as absorbed and effective doses, to a typical patient for a range of available protocols, in a particular CBCT (i-CAT Classic) scanner that is dedicated to dental radiology. In addition, the conversion factors to estimate the effective dose for those protocols were evaluated too.

These studies allow the theoretical estimative of the cancer risk for patients or medical staff, submitted to relatively low doses of radiation, as in radiodiagnosis.

The estimation of the incidence of cancer risk was determined for an organ set, of 35-year-old patients of both genders, exposed to X-rays in CBCT procedures. These individuals were represented by the anthropomorphic adult phantoms, FASH3 (Female Adult MeSH) and MASH3 (Male Adult MeSH) (Cassola et al., 2011).

2. Materials and methods

2.1. Cone beam CT device

This work was performed using a i-Cat classic CBCT scanner (Imaging Sciences International, Hatfield, PA) (Imaging Sciences International, 2010). In this process, the gantry revolves around the individual, in a circular path, emitting beam radiation in every selected FOV. The user can select up to 5 FOV sizes, depending on the purpose of the image, involving the anatomical characteristics of the patient, and the necessary collimation or location. The available options vary according to the chosen protocol. The emission of X-rays is pulsed and controlled by a high-frequency generator. The X-ray tube operates at 120 kVp and 5 mA (in the range 3–7 mA, depending on the installation). The rotation time is 40 s with 3600 acquisitions. The minimum tube filtration was 10 mmAl (120 kV) and the current time product was 36.12 mAs (Imaging Sciences International, 2010). To verify the correct location of the region of interest (ROI), the equipment allows the accomplishment of the scout, with the tube stationary. The distance between the source and the detector was 68.58 cm, and the distance between the source and rotation axis of the equipment (SAD) was 45.72 cm.

2.2. Evaluation of the CBCT unity

Initially, a study of the performance of the simulated equipment, and evaluation of the main physical exposure parameters, was undertaken. A solid-state multi-sensor Rapidose (model RAPD-W sensor, RADCAL® Coorporation) was utilized. This multi-sensor works in the range 40–150 kV and measures the total filtration (up to 22 mmAl), absorbed dose in air, waveform, number of pulses per second, pulse duration, half-value layer, effective time of exposure, among other factors. The multi-sensor was positioned on the radiation tube detector. During the measurement period, the solid-state multi-sensor Rapidose was calibrated, using its Radcal 20272 calibration certificate.

Table 1
Properties of anthropomorphic MASH3 and FASH3 phantoms (Cassola et al., 2011).

Phantom	Mass (kg)	Height (cm)	BMI[a] (kg/m^2)	Matrix (columns × lines × slices)	Voxel dimensions (mm^3)
MASH3	73.0	176.0	23.6	239 × 129 × 731	2.4 × 2.4 × 2.4
FASH3	60.0	163.0	22.7	221 × 128 × 677	2.4 × 2.4 × 2.4

[a] BMI - Body Mass Index.

2.3. Virtual anthropomorphic phantoms

The virtual anthropomorphic phantoms used in this work were the Male Adult meSH (MASH3) and Female Adult meSH (FASH3) (Cassola et al., 2011). They were developed by the *Computational Dosimetry Group of the Department of Nuclear Energy of the Federal University of Pernambuco* (DEN/UFPE). Their characteristics satisfy the recommendations of the International Commission on Radiological Protection, ICRP 89 (Cassola et al., 2010), for the reference anatomical and physiological data of men and women. Table 1 shows some anthropometric data of these phantoms. They have a geometry that represents the internal organs in a very detailed way, which allows results more consistent with the real exams.

2.4. Monte Carlo simulation

In this study, the MC simulation was used to calculate the absorbed dose in a set of organs and tissues. With these values, the effective doses and cancer risk were also determined, for a patient submitted to a dental procedure, using CBCT. The MCNPX 2.7.0 (Pelowitz, 2011) radiation transport code was used to simulate the energy deposition of photons in the organs and tissues of the MASH3 and FASH3 anthropomorphic phantoms. MCNPX code is a MC radiation transport code that operates in a wide range of energies. This version, coupled with a series of codes, was designed nearly sixty years ago at the *Los Alamos National Laboratory*, USA.

This code describes the transport of a set of particles such as photons, electrons, neutrons, nucleons, light ions, beta particles, alpha particles, protons, among other. In addition to these particles, it takes also into consideration the secondary particles, which makes it very attractive for use in various science fields.

The MASH3 and FASH3 phantoms were incorporated into the MCNPX 2.7.0 radiation transport code to represent patients of both genders. During the transport of photons and electrons, the cross section library ENDF/B-VI8 was used to describe the possible effects in the environment. Furthermore, the cut-off values for photons and electrons, interaction type and cross section were maintained as default values of the code, and no variant reduction techniques were employed.

To avoid memory allocation problems with the MCNPX code, and reduce the computational time, the original matrices of phantoms composed of voxels of 1.2 mm in length were resized to 2.4 mm each. This modification reduced the number of voxels, but preserved their physiological and anatomical characteristics. The resizing of the

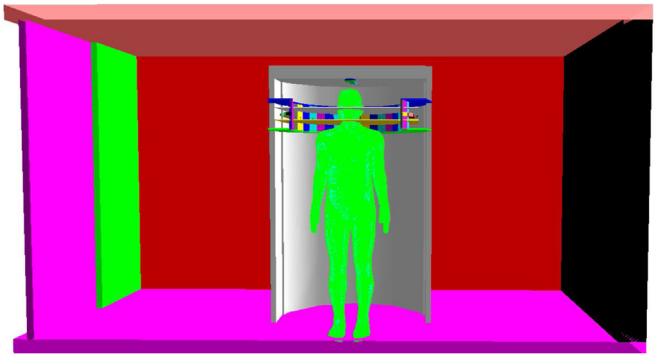

Fig. 1. Irradiation scenario modelled with the MCNPX code composed of a patient performing CBCT exams.

matrices was performed using FANTOMAS digital image processing software (Vieira and Lima, 2009).

All equipment and virtual anthropomorphic phantoms were positioned in a room with dimensions of 2.7 m in length, 4.10 m wide and 2.3 m high. The room was filled with atmospheric air (ρ = 0.001205 g/cm^3) combined by C (0.0124%), N (75.53%), O (23.18%) and Ar (1.28%). The room was composed of concrete walls (ρ = 3.2 g/cm^3) 22 cm thick. Fig. 1 presents the patient computational model exposure.

The X-ray tube was represented by 36-point sources, each one positioned in 10° steps. These photon sources emit beams of radiation in the region of both patient jaws.

The ionization chamber used for the determination of the measured air kerma was a Farmer type ionization chamber (model 10X6-0.6, RADCAL® Coorporation). This chamber has a cylindrical shape and a sensitive volume of 0.6 cm^3. The chamber cavity has a diameter of 0.64 cm and a length of 2.4 cm. The central electrode of the chamber is 2.06 cm long and 0.1 cm in diameter. The wall was made with graphite (0.061 g/cm^2 thick). The rod was modelled with portions of aluminum and graphite, and polytetrafluoroethylene (TEFLON) as insulator (Wulff et al., 2008; Perini et al., 2013). It was positioned in the equipment isocenter. The choice for this device, in relation to the pencil chamber (100 mm), was due to the large FOV used in i-Cat CBCT devices (Stratis et al., 2016). Fig. 2 shows the CBCT equipment, modelled with the MCNPX code, showing the gantry with 36 point sources and the position of the MASH3 virtual anthropomorphic phantom at the exam site.

The selected FOV dimensions were: 8 × 6; 14 × 6; 14 × 8; 14 × 13; and 14 × 22 (cm × cm). A tube peak voltage of 120 kVp, anodic angle of 15°, tungsten target and tube filtration of 13 mmAl were also used. The radiation spectrum was simulated using the SRS 78 spectrum generator software (Cranley et al., 1997). The tube information was obtained by measurements with the RAPIDOSE multisensor (Radcal®), and by the manufacturer manual (Imaging Sciences International, 2010), such as:

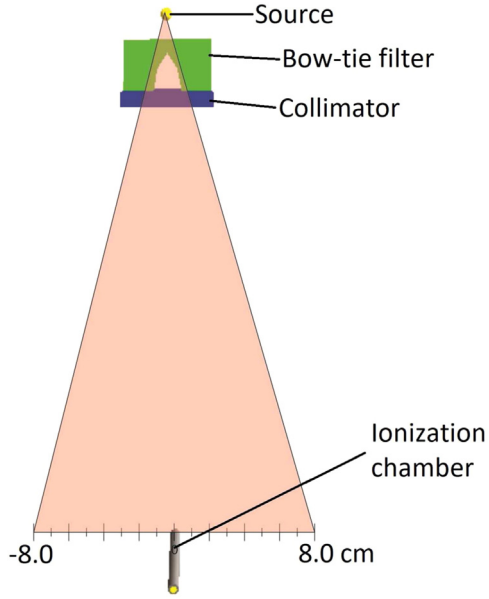

Fig. 3. Scenario for determination of the dose profile produced by the bow-tie filter in the MCNPX code. Figure adapted from Stratis et al. (2016).

tube potential, anodic angle, type and amount of beam filtration and target material of the electron beam. With this information, it was possible to generate the energy spectrum.

To reduce the statistical uncertainties associated with the energy absorbed in organs, tissues and other structures, a total of 1.0 × 10^9 particle histories were used in each scenario.

2.5. Bow-tie filter

The bow-tie filter was constructed to produce a dose profile along the X axis, with the polynomial fit identical to that determined elsewhere (Morant et al., 2012). This profile was reproduced in this work, along the X-axis in ±8 cm from the isocenter (in a total of 17 different positions). Fig. 3 shows the data from Morant et al. (2012), reproduced using MC simulation.

2.6. Conversion factor calculation

For each protocol, a conversion factor (CF), with the unit of particles/mAs (Eq. (1)), was obtained. It was determined by the ratio between the measured air kerma ($K_{air,measured}$ in mGy/mAs) and the simulated air kerma ($K_{MC,simulated\ per\ particle}$ in mGy/particle). The method of definition of the conversion factor, used in this study, was validated in a previous article by Stratis et al. (2016). The simulated air kerma,

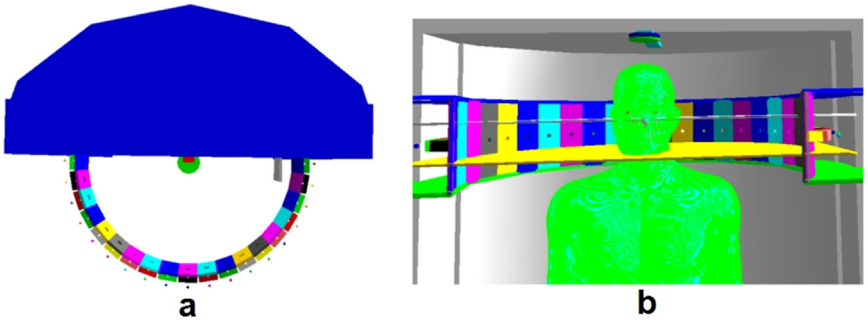

Fig. 2. Computational exposure scenario to simulate a CBCT procedure built for the MCNPX code. a) Gantry with 36 points of sources and; b) Position of the anthropomorphic phantom MASH3 at the exam site.

determined by the MCNP code, was obtained by the *F6* tally (in MeV/g/particle).

In the present study, CF was defined as:

$$CF = \frac{K_{air,measured}}{K_{MC,simulated\ per\ particle}} \quad (1)$$

$K_{air,measured}$ was determined at the isocenter of CBCT device. The measurements were performed with the current-exposure time product of 36.12 mAs. Thus, the unit was mGy/36.12 mAs. $K_{MC,simulated\ per\ particle}$ was obtained under the same conditions of the corresponding protocol, and the parameters reported by the manual and measured in the experimental procedure.

2.7. Absorbed dose

The absorbed dose in tissues/organs, of the anthropomorphic phantoms MASH3 and FASH3, were determined, in the MCNPX code, by means of the Eq. (2) (Gu et al., 2009; Belinato et al., 2015):

$$D_{absolute} = D_{simulated} \times CF \times N \quad (2)$$

where CF is obtained by Eq. (1), $D_{simulated}$ is the value of tally *F6* (in MeV/g/particle), and N = 1, corresponding to only one rotation of the equipment to acquire the image.

2.8. Effective dose

The equivalent dose H_T is defined by $H_T = w_R . D_{(absorbed\ dose)}$. As w_R is the radiation weighting factor (w_R = 1 for X-rays), the equivalent dose will have the same numerical values as the absorbed dose. Then, the effective dose (E) was calculated from Eq. (3), in accordance with the ICRP 110 methodology (ICRP Publication 110, 2009):

$$E = \sum_T w_T \left[\frac{(H_T)_{T,Male} + (H_T)_{T,Female}}{2} \right] \quad (3)$$

where the weighting factor w_T, used for organs and tissues, was taken from the recommendations published by the ICRP 103 (ICRP Publication 103, 2007); $(H_T)_{T,Male}$ and $(H_T)_{T,Female}$ are the equivalent doses of the organs and tissues of male and female anthropomorphic phantoms, respectively.

2.9. Cancer risk

Based on the values of the cancer risk coefficients, provided by BEIR VII (National Research Council, 2006), and the absorbed dose values of each organ and tissue, it was possible to calculate the cancer risk using Eq. (4).

$$R_T = \frac{D_T}{0.1} \cdot r_T \quad (4)$$

where R_T is the incidence cancer risk in 100,000 people exposed to a single dose of 0.1 Gy, D_T is the absorbed dose in Gy in the organ or T-tissue; r_T is the cancer risk factor in the organ or tissue provided by the BEIR VII (National Research Council, 2006).

To quantify the cancer risk (*R*), for a patient submitted to a radiological procedure, it is sufficient to add the cancer risk (R_T) corresponding to each organ or tissue using Eq. (5).

$$R = \sum_T R_T \quad (5)$$

3. Results and discussion

3.1. Evaluation of the CBCT unity

The results regarding the technical performance of the CBCT i-Cat Classic equipment were close to the specifications of the manufacturer's manual. The tube voltage varied 2% relative to the console panel, and with reproducible values for all protocols. The total exposure time presented differences below 5%, compared to the specifications given in the manufacturer's manual. In addition, it was possible to confirm the mode of pulsed exposure, the waveform and HVL (9.2 mmAl). The measured total filtration was 13 mmAl, and the value informed in the manual was just >10 mmAl. The measured pulse time was 17.3 ms with 5.5 μGy. All factors presented reproducibility and constancy in exposures and protocols.

3.2. Bow-tie filter validation

One of the highest challenges of the Monte Carlo simulation, for CBCT scanners, is the information limitations, from the manufacturers, regarding size, shape and materials used to form the beam. An example is the shape and material of the filter used in the X-ray scanner, which directly influences the energy beam.

Without a complete description of this filter, it was considered as a bow-tie filter. The main reason for choosing this filter is justified by the geometry of the target object (head and neck of the individual). This geometry was also chosen due to the methodology used to find the conversion factors (Eq. (1)). According to the study of its validation (Stratis et al., 2016), this method guarantees the applicability of the bow-tie filter. In addition, previous studies by Morant et al. (2013), carried out an equipment from the same manufacturer with similar specifications, and Stratis et al. (2016) have used this filter in simulations of CBCT equipment.

The effect produced by the bow-tie filter can be shown by a curve representing the dose profile at 17 points along the X axis. The simulations for determination of the dose profile of the bow-tie filter used 1E7 particles. Fig. 4 shows a comparison between the dose profile obtained with this study and the dose profile obtained by Morant et al. (2012). This result provided a spatial distribution of the photons in the scenario appropriate to the irradiation conditions of the CBCT studied equipment.

Other universally standardized techniques, such as CTDI, have been discarded in earlier studies (Miracle and Mukherji, 2009; Yu et al., 2010). The main reason was because the CBCT beam is long in the longitudinal direction, and the 100 mm pencil-type ionization chamber is unable to capture all the scattered and generated radiation within the phantom (Miracle and Mukherji, 2009; Yu et al., 2010; Pauwels and Scarfe, 2018).

The use of the dose area product (DAP) is also proposed for conducting MC simulations and dose estimation. However, this technique is limited since some equipment presents a beam with asymmetric geometry, or uses the stitched FOV technique (Pauwels and Scarfe, 2018; Soares et al., 2015b).

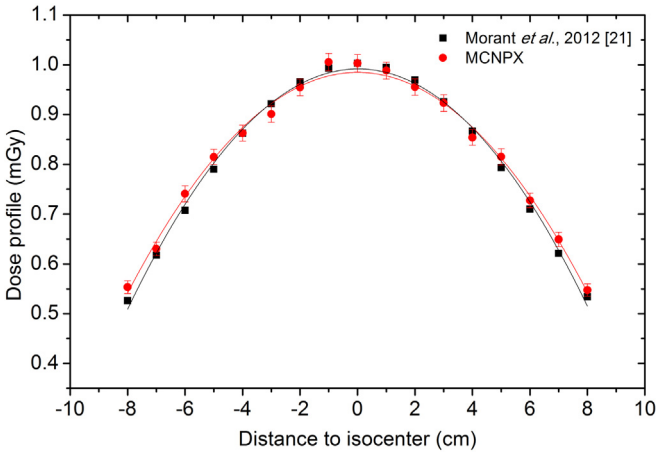

Fig. 4. Dose profile produced by the i-Cat Classic bow-tie filter.

Table 2
Conversion factors (CF) used for the calculation of dose in organs and tissues.

FOV [diameter (cm) × height (cm)]	CF (particle/mAs)
8 × 6	2.34E+11
14 × 6	2.31E+11
14 × 8	1.73E+11
14 × 13	1.07E+11
14 × 22	6.39E+10

3.3. Dose results for CBCT

Table 2 presents the values of the CF as a function of the FOV, which were obtained by the ratio of the measured and the simulated air kerma ($K_{air}/K_{simulated}$). For the studied equipment, K_{air} was 3.409 mGy, and the same irradiation physical parameters were used for all protocols (120 kV tube voltage, 36.12 mAs current-time product, and 13 mmAl filtration).

By means of the CF values presented in Table 2, it was possible to calculate the absorbed doses for each protocol, using Eq. (2). The absorbed dose was calculated for the tissues and organs recommended by ICRP 103 (ICRP Publication 103, 2007), individually, for the MASH3 and FASH3 virtual anthropomorphic phantoms. The results are shown in Table 3. Although the eye lens are not considered for the determination of the effective dose, as recommended by ICRP 103 (ICRP Publication 103, 2007), its absorbed dose were determined for all available protocols. All FOV sizes are conventionally presented as diameter × height (cm × cm).

The highest absorbed dose value was observed for the salivary glands (0.7–2 mGy). The FASH3 phantom received the highest absorbed dose for the 14 cm × 6 cm and 14 cm × 8 cm protocols. The thyroid obtained an expressive value of absorbed dose for the 14 cm × 22 cm protocol (1.94 mGy for FASH3 and 1.30 mGy for MASH3) and lower dose for the 8 cm × 6 cm protocol (0.38 mGy for FASH3 and 0.22 mGy for MASH3). Bone marrow, remainder tissues, oesophagus, bone surface and skin obtained absorbed doses below 0.5 mGy.

The effective dose values of each protocol were determined with Eq. (3) and are presented in Table 3. The effective dose estimative was in the range 75.15–142.20 μSv. The FOV that resulted in the highest effective dose was 14 cm × 22 cm, and the one with the lowest dose was 8 cm × 6 cm.

The increase in the effective dose was proportional to the FOV size. While the FOV increased 43% in diameter and 73% in height, from lowest to highest FOV, the effective dose increased by 47%. Possibly two reasons explain this result: first, the larger FOV encompasses a larger number of radiosensitive organs and, secondly, the larger the FOV, the larger the X-ray scattering to radiosensitive organs, close to the ROI.

From the CF values presented in Table 2, the absorbed doses in the organs and tissues were calculated, and are presented in Table 3. The absorbed doses for the MASH3 and FASH3 virtual anthropomorphic phantoms are similar to bone-marrow, oesophagus, bone surface, brain and skin. Significant absorbed dose values are observed for the salivary glands and thyroid. Pauwels and Scarfe (2018) also draw attention to this fact, where they demonstrate in their studies that the dose is highest in the areas covered by the FOV. Morant et al. (2013) found similar results when comparing female and male phantoms.

The absorbed dose by the FASH3 phantom is greater than for MASH3, especially in the salivary glands, brain and remaining tissues. The difference in absorbed dose between FASH3 and MASH3 are due to the difference in relation to the size of the organs and BMI of both phantoms (Table 1). Absorbed dose values are similar between the two phantoms in bone marrow, bone surface, and skin.

Therefore, there are FOV sizes that for FASH3 will encompass some organs on the primary or near field, increasing the scatter dose absorption, while for MASH3 they are partially enclosed by the region of the primary beam, or by the scattered radiation. This was observed for thyroid and oesophagus, or extrathoracic region, considerably increasing the absorbed dose for the remaining tissues (Table 3). Some studies reminded this fact, indicating the need of avoiding pre-fixed factory protocols (Theodorakou et al., 2012).

The highest absorbed dose for a greater number of tissues and organs occurred for large values of FOV (14 cm × 13 cm and 14 cm × 22 cm). In Table 3 this fact is confirmed, and it is possible to observe a direct and linear relationship between the FOV size and the effective dose. This result is confirmed by other studies that estimated the effective dose, for CBCT, with symmetric geometry beams (Morant et al., 2013; Soares et al., 2015a; Pauwels and Scarfe, 2018; Theodorakou et al., 2012). An indisputable fact is the need for collimation of the radiation beam, reducing the FOV size and assuming the ALARA principle in conducting CBCT exams.

Significant absorbed dose values were observed for the salivary glands and thyroid, as shown in Table 3. This may also be seen in Fig. 5, where the salivary glands correspond to a mean value, for all protocols, of at least 17% of the effective dose. The thyroid corresponds to 27%. They correspond to those doses reported in previous experimental studies (Morant et al., 2013; Soares et al., 2015a; Roberts et al., 2008).

The contribution to the effective dose of the organs and tissues, presented in Fig. 5, is in accordance with previous experimental results (Soares et al., 2015a). Morant et al. (2013) also found similar values in their experimental results when performing this analysis for a CBCT device. When evaluating, in more detail, the mean contribution of

Table 3
Absorbed dose (mGy) in the organs and effective dose (μSv) for MASH3 (M) and FASH3 (F) phantoms.

Organs and tissues	FOV				
	8 cm × 6 cm M/F	14 cm × 6 cm M/F	14 cm × 8 cm M/F	14 cm × 13 cm M/F	14 cm × 22 cm M/F
Bone-marrow (mGy)	0.11/0.12	0.18/0.19	0.16/0.17	0.16/0.17	0.15/0.17
Oesophagus (mGy)	0.03/0.05	0.03/0.05	0.05/0.07	0.06/0.11	0.13/0.24
Thyroid (mGy)	0.22/0.38	0.23/0.38	0.33/0.60	0.50/1.19	1.30/1.94
Bone surface (mGy)	0.07/0.08	0.12/0.12	0.11/0.11	0.10/0.11	0.10/0.11
Brain (mGy)	0.21/0.19	0.41/0.39	0.33/0.31	0.46/0.46	0.71/0.74
Salivary glands (mGy)	0.76/0.82	1.03/2.23	1.95/2.21	1.47/1.61	0.95/1.03
Skin (mGy)	0.06/0.07	0.09/0.11	0.09/0.11	0.09/0.11	0.09/0.11
Remainder Tissues[a] (mGy)	0.18/0.23	0.23/0.28	0.25/0.29	0.20/0.24	0.16/0.19
Effective dose (μSv)[b]	75.15	94.20	105.04	112.05	142.20
Eye Lens (mGy)	0.19/0.21	0.53/0.58	0.23/0.35	0.88/0.96	1.17/1.26

[a] Adrenals, extrathoracic (ET) region, gall bladder, heart, kidneys, lymphatic nodes, muscle, oral mucosa, pancreas, prostate (men), small intestine, spleen, thymus, uterus/cervix (women).
[b] Obtained with Eq. (3).

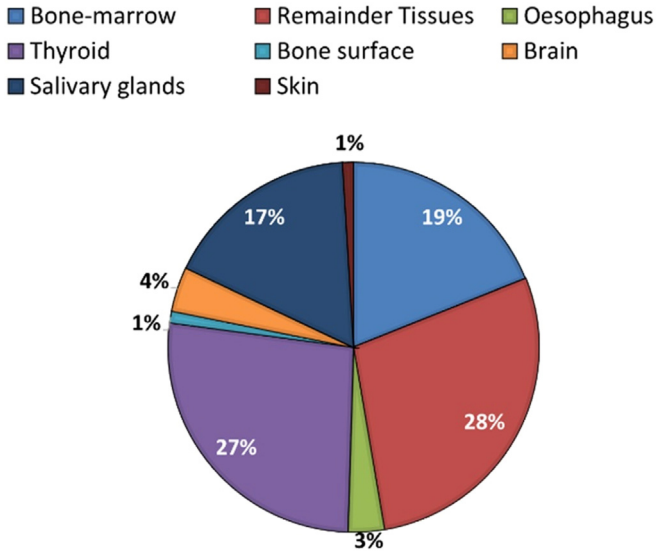

Fig. 5. Contribution of tissues and organs to the effective dose.

tissues and organs to the effective dose (E), a greater prominence was observed for the remainder tissues (28%), salivary glands (17%), thyroid (27%) and bone marrow (19%). Brain, bone surface, oesophagus, and skin presented an effective dose contribution below 5%.

The reason for this high effective dose contribution, to the remainder tissues, is due to the fact that the oral mucosa, and the extrathoracic airways, are effectively within the FOV. Another factor that modifies the contribution of tissues and organs, increasing or decreasing the absorbed dose, is the location of the radiation isocenter (Pauwels and Scarfe, 2018). As the target location is modified, in the buccal cavity, the tissues and organs increase or reduce the dose, according to the established FOV. In this study the FOV was simulated for the anterior part of the mouth, in a 360° rotation. This fact contributes to the justification of these values, since this dose range is common for procedures in other parts of the head.

A highlight in relation to the experimental results is the thyroid. Experimentally, the thyroid presents a contribution of 14% to the effective dose (Soares et al., 2015a). In the present study, a contribution that reached 27% was observed, indicating a higher absorbed dose for protocols with higher FOV sizes.

Although not used for the determination of the effective dose, as suggested by ICRP 103 (ICRP Publication 103, 2007), recent studies suggest that the eye lens radiosensitivity is greater than that suggested by the literature (Pauwels et al., 2014a; ICRP Publication 118, 2012). Furthermore, there is also the somatic effect of radiation to be considered. In this study, the absorbed dose by the eye lens were determined, given its proximity to the ROI. It had a maximum value of 1.26 mGy for FASH3 and 1.17 mGy for MASH3 phantoms, using a 14 cm × 22 cm FOV. For a 14 cm × 13 cm FOV the dose was also significant (0.96 mGy for FASH3 and 0.88 mGy for the MASH3). These data agree with previous studies (Morant et al., 2013; ICRP Publication 118, 2012; Pauwels et al., 2014b), that showed a proportionality between the FOV height and the absorbed dose in the eye lens. A possible solution would be to lower the height of the FOV. However, the ROI and dose increase to the thyroid must also be taken into account. Is is important to note that the thyroid dose was high in this study. As a suggestion to the users, is to review the exam parameters, as tube voltage, current, exposure time, beam geometry, and the capability of CBCT equipment to allow FOVs with personalized sizes, to the clinical need of the image, always taking into account the image quality.

Undoubtedly, analyzing the data, especially of Tables 3 and 4, it was possible to realize the need for optimization of the radiation doses for exposure during CBCT procedures. The main points are technical factors, where an optimization of the pre-established protocols is emphasized, mainly for young people and children. A second highlight, from Table 3, is the delimitation of the FOV size. A final point is the use of individual protection, considering that it does not interfere in the image quality.

3.4. Cancer risk

The health risks attributable to exposure to ionizing radiation depend on the absorbed dose in the organ, the type of irradiated organ, age and gender of the exposed individuals. Knowing the absorbed dose of each organ/tissue and using the values of appropriate cancer induction risk coefficients, it was possible to calculate the risks of induction of cancer of a set of organs and tissues of the patient. The main results of cancer risk of organs and tissues, and the effective risk (R) according to gender and FOV, attributable to a total of 100,000 people, with an average age of 35 years, are presented in Table 4. The cancer risk results for leukemia were obtained by the absorbed dose values, in the red bone marrow, and the results for the others organs/tissues correspond to the set of other organs defined by ICRP 103 (ICRP Publication 103, 2007).

Among the evaluated organs of the patient, it was observed that the cancer risks in the red bone marrow (leukemia), lungs, and remainder tissues presented high values. Important differences in cancer risk were observed between the MASH3 and FASH3 organs. For most organs located far from the primary radiation beam, such as the colon, stomach, bladder and liver, the values were lower, when compared to those organs located closer to the FOV, such as the thyroid, breasts and lungs. It may also be notet that the effective cancer risk was higher for the female gender, for all FOV considered in this work. This difference is mainly due to the risk of breast and gonads cancer.

The present calculations showed that for a typical CBCT procedure, the cancer risk for women, in the same exposure conditions, can exceed by 26–34% the values for men.

Even with the limitations of the stochastic effects in CBCT, studies stated that women, young and children receive a high dose (Theodorakou et al., 2012). For people over the age of 60 the cancer risk is four times lower than for children (Pauwels et al., 2014b). In this sense, it is necessary to evaluate the need to carry out the examination, and, when possible, to use specific protocols for children (Soares et al., 2015a; Pauwels and Scarfe, 2018). It should be noted, however, that other radiological exams may be also efficient for the clinical objective.

4. Conclusions

The results obtained in this study point to an adequate methodology to determine the doses in dental CBCT from air kerma measurements. The CF values indicate that the larger the radiation field, higher will be the absorbed and effective doses. This fact is justified by the number of tissues and organs irradiated when the field size increases. Ultimately, as the number of patients using this type of exam tends to grow, it is expected that the absorbed and effective doses presented in this study will enable the medical staff to better manage the doses to the patients. The MC method was used to estimate the absorbed dose in tissues and organs, as well as the effective dose and cancer risk, for a female and a male virtual anthropomorphic phantoms. The parameters used in the simulation are used routinely, and they were compared with previously published experimental results. Higher values of absorbed dose were observed in the thyroid and salivary glands. Using the absorbed dose values of each organ and tissue, it was possible to calculate the cancer risk for a set of organs and tissues of a patient submitted to a typical CBCT examination. The results indicate that for the same exposure conditions, women can exceed the total risk of cancer by 26–34%, when compared to men. This difference may be attributed to the contribution from the FASH3 breasts and gonads.

Table 4
Number of cancer incidence cases for a set of organs and tissues of the male (MASH3) and female (FASH3) genders and the total risk (R) for the typical CBCT procedure. The values show the number of cases per 100,000 people.

	Number of cancer incidence cases/FOV				
Organs	8 cm × 6 cm	14 cm × 6 cm	14 cm × 8 cm	14 cm × 13 cm	14 cm × 22 cm
MASH3					
Bone-marrow	1.1E−02	1.8E−02	1.6E−02	1.6E−02	1.5E−02
Colon	9.4E−05	1.0E−04	8.9E−05	7.1E−05	6.9E−05
Lung	2.2E−03	2.6E−03	3.4E−03	4.0E−03	6.8E−03
Stomach	4.8E−05	5.7E−05	5.9E−05	5.9E−05	7.6E−05
Remainder tissues[a]	4.0E−02	5.2E−02	5.5E−02	4.5E−02	3.5E−02
Bladder	4.6E−06	6.2E−06	4.2E−06	3.2E−06	2.8E−06
Liver	2.0E−05	2.5E−05	2.6E−05	2.7E−05	3.6E−05
Thyroid	5.3E−04	5.5E−04	8.0E−04	1.2E−03	3.1E−03
Effective risk	5.3E−02	7.2E−02	7.5E−02	6.5E−02	5.7E−02
FASH3					
Bone-marrow	9.1E−03	1.4E−02	1.3E−02	1.3E−02	1.3E−02
Colon	8.6E−05	9.7E−05	8.7E−05	7.5E−05	8.0E−05
Lung	8.1E−03	9.8E−03	1.2E−02	1.5E−02	2.8E−02
Stomach	1.0E−04	1.2E−04	1.4E−04	1.4E−04	1.8E−04
Breast	2.3E−03	3.2E−03	3.2E−03	2.9E−03	2.9E−03
Remainder tissues[a]	5.2E−02	6.6E−02	6.7E−02	5.5E−02	4.3E−02
Gonads	4.1E−06	1.9E−06	5.1E−06	3.8E−06	4.4E−06
Bladder	5.9E−06	6.3E−06	5.2E−06	4.3E−06	4.0E−06
Liver	1.4E−05	1.9E−05	2.0E−05	2.1E−05	2.8E−05
Thyroid	4.2E−03	4.1E−03	6.6E−03	1.3E−02	2.1E−02
Effective risk	7.2E−02	9.3E−02	9.6E−02	8.6E−02	8.7E−02

[a] Remainder Tissues: Adrenals, Extrathoracic (ET) region, Gall Bladder, Heart, Kidneys, Lymphatic nodes, Muscle, Oral mucosa, Pancreas, Ovaries, Small intestine, Spleen, Thymus, Uterus.

Acknowledgments

The authors would like to thank Dr. Richard Kramer for kindly providing the virtual anthropomorphic phantoms. This work was partially supported by the Brazilian agencies: Fundação de Amparo à Pesquisa do Estado de Minas Gerais (FAPEMIG, Grants nos. APQ-03049-15 and APQ-02934-15) and Conselho Nacional de Desenvolvimento Científico e Tecnológico (CNPq, Grants nos. 421603/2016-0, 420699/2016-3, 168947/2017-0 and 301335/2016-8).

References

Abramovitch, K., Rice, D.D., 2014. Radiation dosimetry in digital breast tomosynthesis: report of AAPM Tomosynthesis Subcommittee Task Group 223. Dent. Clin. N. Am. 58 (3), 463–484. https://doi.org/10.1016/j.cden.2014.03.002.

Belinato, W., Santos, W.S., Paschoal, C.M.M., Souza, D.N., 2015. Monte Carlo simulations in multi-detector CT (MDCT) for two PETCT scanner models using MASH and FASH adult phantoms. Nucl. Instrum. Methods Phys. Res. Sect. A: Accel. Spectrom. Detect. Assoc. Equip. 784 (1), 524–530. https://doi.org/10.1016/j.nima.2014.09.036.

Cassola, V.F., Kramer, R., Brayner, C., Khoury, H.J., 2010. Posture-specific phantoms representing female and male adults in Monte Carlo-based simulations for radiological protection. Phys. Med. Biol. 55 (15), 4399–4430. https://doi.org/10.1088/0031-9155/55/15/014.

Cassola, V.F., Milian, F.M., Kramer, R., de Oliveira Lira, C.A., Khoury, H.J., 2011. Standing adult human phantoms based on 10th, 50th and 90th mass and height percentiles of male and female Caucasian populations. Phys. Med. Biol. 56 (1), 3749–3772. https://doi.org/10.1088/0031-9155/56/13/002.

Cranley, K., Gilmore, B., Fogarty, G., Despond, L., 1997. Catalogue of Diagnostic X-ray Data and Other Data. Tech. Rep. 78. Institute of Physics and Engineering in Medicine (IPEM), London.

Gu, J., Bednarz, B., Caracappa, P.F., Xu, X.G., 2009. The development, validation and application of a multi-detector CT (MDCT) scanner model for assessing organ doses to the pregnant patient and the fetus using Monte Carlo simulations. Phys. Med. Biol. 54 (9), 2699–2717. https://doi.org/10.1088/0031-9155/54/9/007.

ICRP Publication 10, 2007. The 2007 recommendations of the international commission on radiological protection. Annal 37 (24).

ICRP Publication 110, 2009. Adult reference computational phantoms. Ann. ICR 39 (2).

ICRP Publication 118, 2012. ICRP statement on tissue reactions/early and late effects of radiation in normal tissues and organs - threshold doses for tissue reactions in a radiation protection context. Ann. ICRP 41 (1–2).

Imaging Sciences International, 2010. Operator's Manual – Cone Beam Volumetric Tomography and Panoramic Dental Imaging System. Tech. Rep. Part number 990310 – Rev A. Imaging Sciences International, Hatfield, PA.

Koivisto, J., Wolff, J., Järnstedt, J., Dastidar, P., Kortesniemi, M., 2014. Assessment of the effective dose in supine, prone, and oblique positions in the maxillofacial region using a novel combined extremity and maxillofacial cone beam computed tomography scanner. Oral Surg. Oral Med. Oral Pathol. Oral Radiol. 118 (3), 355–362. https://doi.org/10.1016/j.oooo.2014.05.016.

Miracle, A.C., Mukherji, S.K., 2009. Conebeam ct of the head and neck, part 1: physical principles. Am. J. Neuroradiol. 30 (6), 1088–1095. https://doi.org/10.3174/ajnr.A1653.

Morant, J., Salvadó, M., Casanovas, R., Hernández-Girón, I., Velasco, E., Calzado, A., 2012. Validation of a monte carlo simulation for dose assessment in dental cone beam ct examinations. Phys. Med. 28 (3), 200–209. https://doi.org/10.1016/j.ejmp.2011.06.047.

Morant, J.J., Salvadó, M., Hernández-Girón, I., Casanovas, R., Ortega, R., Calzado, A., 2013. Dosimetry of a cone beam ct device for oral and maxillofacial radiology using monte carlo techniques and ICRP adult reference computational phantoms. Dentomaxillofac Radiol. 42 (3), 92555893. https://doi.org/10.1259/dmfr/92555893.

Mozzo, P., Procacci, C., Tacconi, A., Martini, P.T., Andreis, I.A., 1998. A new volumetric ct machine for dental imaging based on the cone-beam technique: preliminary results. Eur. Radiol. 8 (9), 1558–1564.

National Research Council, 2006. Health Risks from Exposure to Low Levels of Ionizing Radiation: BEIR VII Phase 2. The National Academies Press, Washington, DC. https://doi.org/10.17226/11340.

Pauwels, R., Scarfe, W.C., 2018. Radiation dose, risks, and protection in CBCT. In: Scarfe, W.C., Angelopoulos, C. (Eds.), Maxillofacial Cone Beam Computed Tomography – Principles, Techniques and Clinical Applications. Springer, Cham, New York, NY 10013, USA, pp. 227–246. https://doi.org/10.1007/978-3-319-62061-9_8.

Pauwels, R., Zhang, G., Theodorakou, C., Walker, A., Bosmans, H., Jacobs, R., Bogaerts, R., Horner, K., SEDENTEXCT Project Consortium, 2014. Effective radiation dose and eye lens dose in dental cone beam CT: effect of field of view and angle of rotation. Br. J. Radiol. 87 (1042), 20130654. https://doi.org/10.1259/bjr.20130654.

Pauwels, R., Cockmartin, L., Ivanauskaité, D., Urbonienė, A., Gavala, S., Donta, C., Tsiklakis, K., Jacobs, R., Bosmans, H., Bogaerts, R., Horner, K., SEDENTEXCT Project Consortium, 2014. Estimating cancer risk from dental cone-beam CT exposures based on skin dosimetry. Phys. Med. Biol. 59 (14), 3877–3891. https://doi.org/10.1088/0031-9155/59/14/3877.

Pelowitz, D.B., 2011. MCNPX User's Manual. Version 2.7.0, Report LA-CP-11-0043. Los Alamos National Laboratory, Oak Ridge.

Perini, A.P., Neves, L.P., Fernández-Varea, J.M., Büermann, L., Caldas, L.V.E., 2013. Evaluation and simulation of a new ionization chamber design for use in computed tomography beams. IEEE Trans. Nucl. Sci. 60 (2), 768–773. https://doi.org/10.1109/TNS.2012.2233752.

Qu, X.M., Li, G., Ludlow, J.B., Zhang, Z.Y., Ma, X.C., 2010. Effective radiation dose of ProMax 3D cone-beam computerized tomography scanner with different dental protocols. Oral Surg. Oral Med. Oral Pathol. Oral Radiol. Endodontol. 110 (6), 770–776. https://doi.org/10.1016/j.tripleo.2010.06.013.

Roberts, J.A., Drage, N.A., Davies, J., Thomas, D.W., 2008. Effective dose from cone beam ct examinations in dentistry. Br. J. Radiol. 82 (973), 35–40. https://doi.org/10.1259/bjr/31419627.

Rottke, D., Patzelt, S., Poxleitner, P., Schulze, D., 2013. Effective dose span of ten different cone beam ct devices. Dentomaxillofacial Radiol. 42 (7), 20120417. https://

doi.org/10.1259/dmfr.20120417.
Scarfe, W.C., Li, Z., ans, W.A., Scott, S.A., Farman, A.G., 2012. Maxillofacial cone beam computed tomography: essence, elements and steps to interpretation. Aust. Dent. J. 57 (1), 46–60. https://doi.org/10.1111/j.1834-7819.2011.01657.x.
Soares, M.R., Batista, W.O., Antonio, P.L., Caldas, L.V.E., Maia, A.F., 2015a. Study of effective dose of various protocols in equipment cone beam ct. Appl. Radiat. Isot. 100, 21–26. https://doi.org/10.1016/j.apradiso.2015.01.012.
Soares, M.R., Batista, W.O., Antonio, P.L., Caldas, L.V.E., Maia, A.F., 2015b. Effective dose comparison between stitched and single FOV in CBCT protocols for complete dental arcade. Radiat. Phys. Chem. 110, 72–76. https://doi.org/10.1016/j.radphyschem.2015.01.019.
Stratis, A., Zhang, G., Lopez-Rendon, X., Jacobs, R., Bogaerts, R., Bosmans, H., 2016. Customisation of a Monte Carlo dosimetry tool for dental cone-beam CT systems. Radiat. Prot. Dosim. 169 (1–4), 378–385. https://doi.org/10.1093/rpd/ncw024.
Theodorakou, C., Walker, A., Horner, K., Pauwels, R., Bogaerts, R., Jacobs, R., SEDENTEXCT Project Consortium, 2012. Estimation of paediatric organ and effective doses from dental cone beam CT using anthropomorphic phantoms. Br. J. Radiol. 85 (1010), 153–160. https://doi.org/10.1259/bjr/19389412.
Vieira, J.W., Lima, F.R.A., 2009. A software to digital image processing to be used in the voxel phantom development. Cell. Mol. Biol. 55 (3), 16–22.
Wulff, J., Heverhagen, J.T., Zink, K., 2008. Monte-Carlo-based perturbation and beam quality correction factors for thimble ionization chambers in high-energy photon beams. Phys. Med. Biol. 53 (11), 2823–2836. https://doi.org/10.1088/0031-9155/53/11/005.
Yu, L., Vrieze, T.J., Bruesewitz, M.R., Kofler, J.M., Delone, D.R., Pallanch, J.F., Lindell, E.P., McCollough, C.H., 2010. Dose and image quality evaluation of a dedicated cone-beam CT system for high-contrast neurologic applications. Am. J. Roentgenol. 194 (2), W193–201. https://doi.org/10.2214/AJR.09.2951.